

Field-Induced Lifshitz Transition in the Magnetic Weyl Semimetal Candidate PrAlSi

Lei Wu¹, Shengwei Chi¹, Huakun Zuo¹, Gang Xu¹, Lingxiao Zhao^{2,*}, Yongkang Luo^{1,*}, Zengwei Zhu^{1,*}

(1) *Wuhan National High Magnetic Field Center and School of Physics,*

Huazhong University of Science and Technology,

Wuhan 430074, China

(2) *Department of Physics,*

Southern University of Science and Technology,

Shenzhen 518055, China

(Dated: January 23, 2023)

Lifshitz transition (LT) refers to an abrupt change in the electronic structure and Fermi surface, and is associated to a variety of emergent quantum phenomena. Amongst the LTs observed in known materials, the field-induced LT has been rare and its origin remains elusive. To understand the origin of field-induced LT, it is important to extend the material basis beyond the usual setting of heavy fermion metals. Here, we report on a field-induced LT in PrAlSi, a magnetic Weyl semimetal candidate with localized $4f$ electrons, through a study of magnetotransport up to 55 T. The quantum oscillation analysis reveals that across a threshold field $B^* \approx 14.5$ T the oscillation frequency ($F_1 = 43$ T) is replaced by two new frequencies ($F_2 = 62$ T and $F_3 = 103$ T). Strikingly, the LT occurs well below quantum limit, with obvious temperature-dependent oscillation frequency and field-dependent cyclotron mass. Our work not only enriches the rare examples of field-induced LTs, but also paves the way for further investigation on the interplay among topology, magnetism and electronic correlation.

The Lifshitz transition (LT) has received renewed attention in the condensed matter physics. A LT [1] is an electronic topological transition of the Fermi surface (FS) driven by the variation of the band structure and/or the Fermi energy. Since such a transition does not necessarily require simultaneous symmetry breaking, and meanwhile, it can occur at $T = 0$, be tuned by parameters other than temperature (such as pressure, strain, doping, magnetic field etc.) [1, 2], it, therefore, can be deemed as a topological quantum phase transition. In the vicinity of Lifshitz transitions, many peculiar emergent phenomena may appear, such as van-Hove singularity, non-Fermi-liquid behavior, unconventional superconductivity and so on (e.g. [3, 4]).

Compared with a number of cases tuned by doping or pressure that have been widely seen in topological systems [5, 6], cuprate superconductors [7, 8], iron pnictides superconductors [9, 10], and other strongly correlated materials [3, 11], the examples of LT driven by magnetic field are rare. This is because the energy scale of a laboratory magnetic field, in the order of 1-10 meV, is much smaller than the characteristic energy scale of most metals ($\sim 10^2 - 10^3$ meV). Only in a few cases, mostly limited in heavy-fermion (HF) metals [2, 13–20], the hybridization between conduction electrons and localized f electrons leads to narrow renormalized bands with a small Fermi energy and thus the Zeeman term can be sufficiently strong to shift the spin-split FS [15]. Recently, field-induced LTs were also observed in some low Fermi energy non-magnetic semimetals such as bismuth [21], TaP [22] and TaAs [23], wherein magnetic field beyond quantum limit can empty a Dirac or Weyl pocket with small Fermi energy. However, in these cases, no additional Fermi pocket emerges and the carriers of the empty pocket were transferred to other pockets (pre-

viously existing).

Here we present a new example of field-induced LT beyond heavy-fermion systems in the magnetic Weyl semimetal candidate PrAlSi, by a systematic study of quantum oscillation (QO) effect with the magnetic field extending up to 55 T. We observe a single frequency ($F_1 = 43$ T) below a critical field of $B^* = 14.5$ T, in agreement with what was previously reported [24]. Above B^* , we see clearly the emergence of two new frequencies ($F_2 = 62$ T and $F_3 = 103$ T) and the disappearance of the original F_1 . We exclude the possibility of magnetic breakdown and identify B^* as a critical point where the field-induced LT occurs. By comparing the reported Fermi surface of NdAlSi and theoretical calculation of PrAlSi, we conclude that the LT occurs in the hole-like Weyl pockets along the direction of Γ -X of the Brillouin zone (BZ, hereafter). Our work not only enriches the rare examples of field-induced LTs, but also paves the way for further investigation on the interplay among topology, magnetism and electronic correlation.

The $RAlX$ family (R = rare earth and X = Si or Ge) compounds have recently been proposed to host ideal candidates of magnetic Weyl semimetals [25, 26], and provide a platform to investigate the interaction between magnetism and Weyl physics [27–31]. They crystallize in a tetragonal structure with the noncentrosymmetric space group symmetry of $I4_1/md$ (No. 109). One advantage of this family is that Weyl nodes generated by inversion breaking are robust and can be shifted by the Zeeman coupling in the k space [25]. Several intriguing physical properties have been observed in this family. The list includes the coexistence of type-I and type-II Weyl fermion in LaAlSi [32] and LaAlGe [33], topological Hall effect in CeAlGe [34], anisotropic anomalous Hall effect in CeAlSi [35], and Weyl-driven collective magnetism

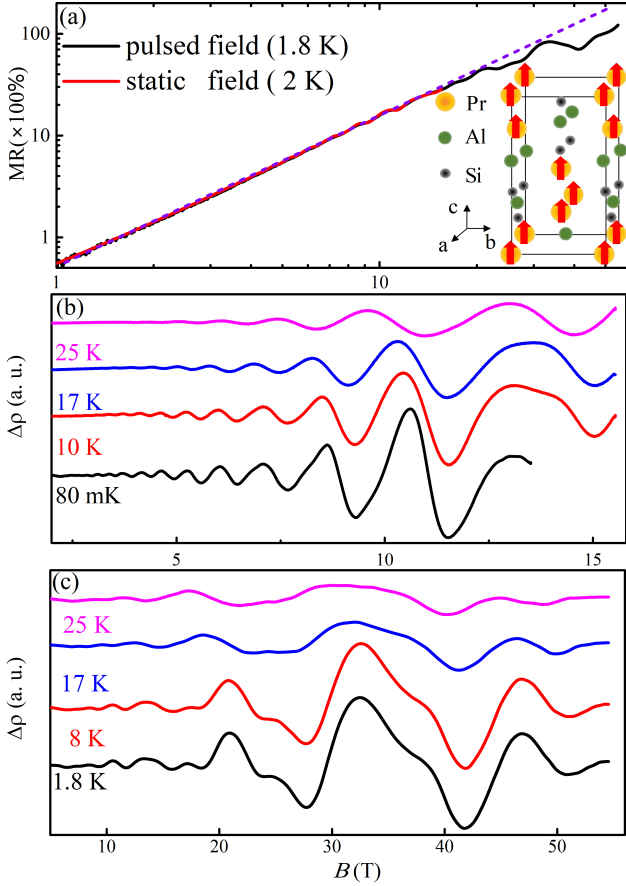


FIG. 1. (a) The field-dependent of MR measured under static field at 2 K and pulsed field at 1.8 K. The inset is crystal structure ($I4_1/m\bar{d}$) of PrAlSi as the magnetic field easily polarizes the moments of Pr along the c -axis. (b) Field dependence of the oscillatory part of magnetoresistance $\Delta\rho(B)$ in low magnetic field measured under static field, showing only a single QO frequency. The experiments were carried out with a Leiden dilution refrigerator (14 T) at 80 mK and with a refrigerator of Oxford Instrument (16 T) at $T = 10$ K, 17 K and 25 K. (c) $\Delta\rho(B)$ in high magnetic field measured by pulsed magnetic field, showing more QO frequencies with a complex pattern.

in NdAlSi [36]. The compound PrAlSi studied here is a ferromagnetic semimetal with Curie temperature $T_C \sim 18$ K. A recent work based on static field (9 T) transport measurements by Lyu et al. revealed a large anomalous Hall conductivity $\sim 2000 \Omega^{-1}\text{cm}^{-1}$ and an unusual temperature dependence of QO with a single frequency [24].

High-quality single crystals of PrAlSi were synthesized using the flux method. The inset of Fig. 1(a) shows the crystal structure of PrAlSi with the magnetic moments of Pr easily orientated along c -axis after the application of a small field [24]. In our transport measurements, the magnetic field was along the c -axis and the electrical current was along the b -axis (more details are presented in METHODS and Supplemental Material). Fig. 1(a) shows magnetoresistance measured in static field at

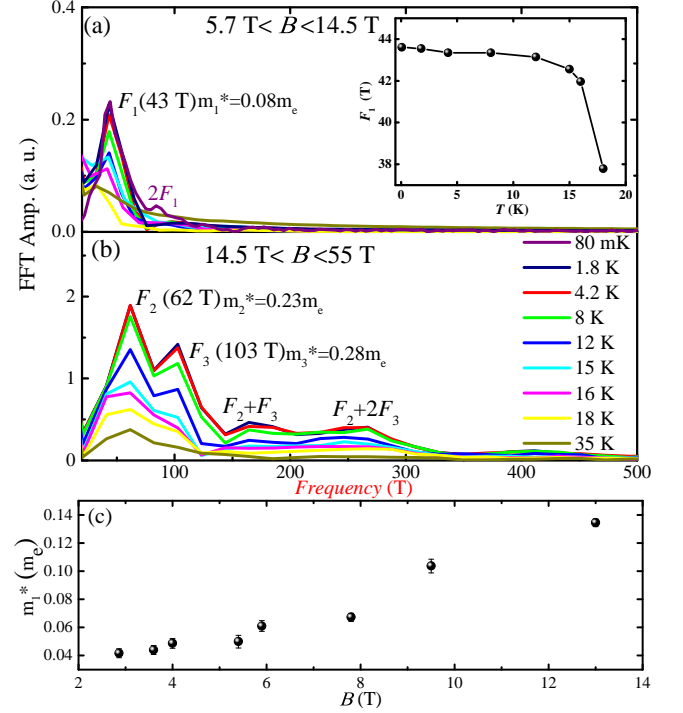


FIG. 2. (a)(b) The frequency (T) dependence of the fast-Fourier-transformation amplitude of SdH oscillations measured at various temperatures with $B \parallel c$ in pulsed field. With the field lower than 14.5 T, only one fundamental frequency exists in (a). Two main higher frequencies and harmonic terms are shown in (b) with the field above 14.5 T. The inset shows the temperature-dependent frequency F_1 extracted from (a). (c) The corresponding effective mass of F_1 as a function of magnetic field B obtained from the analysis of the QO peaks in static field.

2 K (red curve) and pulsed field at 1.8 K (black curve). Normalized magnetoresistance $(\rho(B) - \rho(0))/\rho(0)$ reaches 116 at 55 T and remains non-saturating. The purple dashed line corresponds to $B^{1.7}$. Fig. 1(b) presents the oscillatory part of the longitudinal resistivity $\Delta\rho(B)$, obtained by subtracting a smooth background from the measured $\rho(B)$ (see the Supplementary Figure 2 for more raw data). At low temperature, oscillations are visible above the field as low as 3 T, indicating the good quality of the sample. The rough Dingle mobility of $1/B_c = 0.33 \text{ T}^{-1}$ is close to the average mobility of $0.26 \text{ m}^2/\text{Vs}$ yielded from the amplitude of the quadratic low-field magnetoresistance (see the inset of the Supplementary Figure 2 (a)). The single-frequency QO for static field measurements retains until temperature down to 80 mK. A more complex pattern emerges when larger magnetic field is applied, as seen in Fig. 1(c).

Fig. 2(a) and (b) show the results of the fast Fourier transformation (FFT) of the oscillatory part of the magnetoresistance $\Delta\rho$ as a function of $1/B$. The SdH frequencies extracted from low-field ($B < 14.5$ T) and high-field ($B > 14.5$ T) data display a dramatic difference. Note that, since this compound is ferromagnetic, we took

into the demagnetization factor to correct the applied field in all the analyses of SdH effect (see the Section 9 of the Supplemental Material). We identified $B^* = 14.5$ T as a critical field, after checking several fields close to B^* . As shown in the Supplementary Figure 3, we have intercepted a field with different values, 10, 14, 14.5, 15 and 20 T for the segmented FFT analyses. We can see the crossover from the lower QO frequency to the two higher QO frequencies as the segment changes between the 5.7 T and the selected field. Two higher QO peaks emerge when we segment the field at 20 T and we note that the low QO peaks persist because of the inclusion of the low-field QOs below 14.5 T. From the comparison of the segmented FFT analyses, 14.5 T was determined as the field of the LT. There is only one fundamental frequency in the FFT spectrum until down to 80 mK below B^* , see Fig. 2(a). It should be noted that F_1 gradually decreases with temperature, changing from 43 T at 80 mK to 32 T at 35 K, as shown in the inset. Similar temperature dependence in F_1 was also reported in an earlier work on PrAlSi[24], whereas the values of F_1 are relatively smaller than ours. We attribute this discrepancy to the difference in stoichiometry[19].

Fig. 2(b) shows that above B^* there are two new QO frequencies ($F_2 = 62$ T, $F_3 = 103$ T) and their high-order harmonics. Such a change in Fermi surface is also manifested in the effective cyclotron mass m^* . The value of m^* for each frequency can be deduced from the fitting of FFT amplitude according to the temperature damping factor, and this yields the small $m^* = 0.08 m_e$ for F_1 (with field range 5.7-14.5 T), and $0.23 m_e$ and $0.28 m_e$ for F_2 and F_3 , respectively, where m_e is the mass of a free electron. Interestingly, a careful look into the temperature dependence of the amplitude of the oscillatory peak leads to the fact that the effective mass is enhanced 2-fold between 2.8 T and B^* , as shown in Fig. 2(c). This feature is reminiscent of HF systems displaying a LT, and will be discussed more later on. The effective masses of F_2 and F_3 as the function of field higher than B^* are absent here, mainly because it's rather difficult to extract the exact amplitude of entangled peaks in oscillatory part from two frequencies and their harmonic terms. More explanation about effective mass mentioned above is exhibited in Supplementary Figure 5. The Fermi energy of the band corresponding to F_1 is then estimated $\varepsilon_F \sim 125$ meV.

To further demonstrate the field-induced Fermi surface change near $B^* = 14.5$ T, we performed Lifshitz-Kosevich (LK) fitting on $\Delta\rho(B)$ measured under pulsed field. We notice that all the analyzed FFT data are from the pulsed fields. More details can be found in Section 4 of the Supplemental Material. As is shown in Fig. 3(a), the $\Delta\rho$ for field below B^* can be well reproduced by the LK fitting with a single F_1 (cf. the red dot line). However, such a fitting collapses when field exceeds B^* . This problem can be fixed in an alternate fitting by employing both F_2 and F_3 , seeing the blue dot line in Fig. 3(b). Noteworthy that this 2-frequency LK fitting fails in the low-field window,

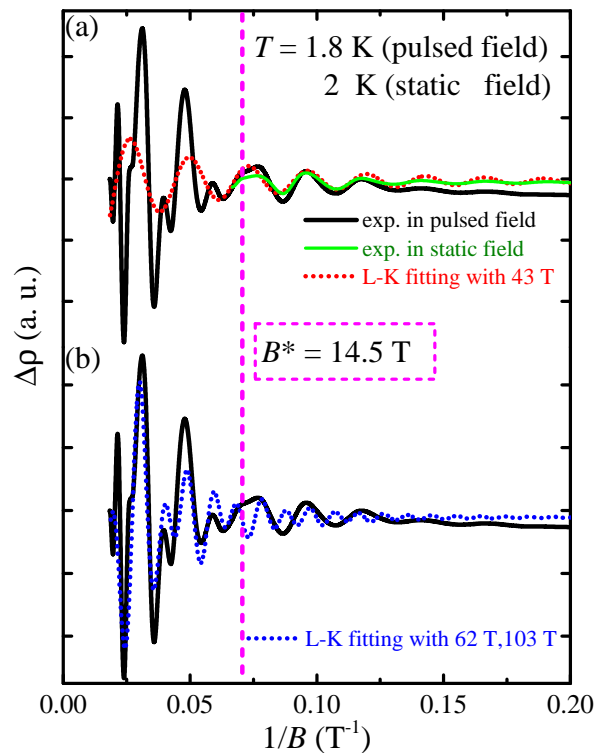


FIG. 3. The Lifshitz-Kosevich fit to $\Delta\rho(B)$ measured with pulsed field. Inverse field dependence of the oscillatory magnetoresistance measured at 1.8 K with pulsed field and at 2 K with static field are depicted as black and green lines, respectively. Note that the L-K fitting with a single frequency of 43 T reproduces the SdH oscillations nicely for field below B^* , but fails for $B > B^*$, as shown in panel (a). A multi-frequency L-K fitting by employing both F_2 and F_3 describes $\Delta\rho(B)$ reasonably well for $B > B^*$, seeing panel (b).

implying that F_2 and F_3 appear only in the high-field range.

Thus, the variation of QO frequencies with the disappearance of 43 T and the emergence of 62 T and 103 T clearly point to the change in Fermi surface topology, viz a LT. Firstly, we can rule out magnetic breakdown as the origin, because there is no extra QO frequency (19 T and 60 T) in the low-field range even for temperature as low as 80 mK. Moreover, the peak with frequency of 43 T does not persist under high magnetic field, either. Secondly, we can also exclude a metamagnetic transition as the driver of this process. Fig. 4(a) shows the field dependence of magnetization at 2 K with the magnetic field applied along c -axis. One clearly finds that the magnetization saturates to $\sim 3.1 \mu_B/\text{Pr}$ at a small field 0.48 T, and no additional transition can be resolved nearby 14.5 T except for some traces of de Haas-van Alphen oscillations (inset of Fig. 4(a)). This is different from the case of NdAlSi, where a magnetic transition to the final Weyl-mediated helical magnetism leads to a change in QO frequency [36].

In order to further clarify this field-induced LT, it is

helpful to estimate the density of carriers of each Fermi pocket. According to the Lifshitz-Onsager relation, $F = (\hbar/2\pi e)A_F$, where \hbar is Planck's constant and $A_F = \pi k_F^2$ is an extremal cross-sectional area of the Fermi surface perpendicular to the field with Fermi wave vector k_F . The bands become non-degenerate due to spin-orbit coupling[36]. Assuming these Fermi pockets are spheres, we find that the LT wipes out $n_{F_1} = 3.2 \times 10^{18} \text{ cm}^{-3}$ and produces $n_{F_2} = 5.5 \times 10^{18} \text{ cm}^{-3}$ and $n_{F_3} = 1.2 \times 10^{19} \text{ cm}^{-3}$ per 4 pockets. Note that the total number of pockets would be a multiple of four, due to the symmetric requirement (see below).

The *total* carrier density of hole and electron can be also extracted by fitting the Hall resistivity to a two-band model, $\rho_{xy}(B) = \frac{B}{e} \frac{(n_h \mu_h^2 - n_e \mu_e^2) + \mu_h^2 \mu_e^2 (n_h - n_e) B^2}{(n_h \mu_h + n_e \mu_e)^2 + \mu_h^2 \mu_e^2 (n_h - n_e)^2 B^2}$. Here, n and μ represent carrier density and mobility, respectively. We obtain $n_h = 4.3 \times 10^{19} \text{ cm}^{-3}$, $n_e = 5.3 \times 10^{19} \text{ cm}^{-3}$, $\mu_h = 0.18 \text{ m}^2/\text{Vs}$ and $\mu_e = 0.22 \text{ m}^2/\text{Vs}$. These values fit both Hall resistivity and magnetoresistivity reasonably well up to B^* (see Fig. 4(c) and Supplementary Figure 7). The deduced mobilities are also close to the value obtained from quantum oscillations and magnetoresistance. The average zero-field mobility $\langle \mu \rangle$ extracted from the residual resistivity $\rho_0 = 15 \mu\Omega \cdot \text{cm}$ is about $0.5 \text{ m}^2/\text{Vs}$, slightly larger than the finite-field mobility. Such a discrepancy has been observed in other semimetals[37, 38] and attributed to the field-induced mobility reduction. The carrier densities of hole and electron are within 10% of the compensation $2[n_e n_h / (n_e + n_h)]$, compared to $\sim 4\%$ in bismuth[39] and WTe₂[40]. This near compensation would explain the observed unsaturated magnetoresistance. The slight excess in hole may result from an uncontrollable doping which could be also the reason for the sample dependence of F_1 as discussed above.

This fit, which properly works up to B^* (shown by a black arrow in Fig. 4(c)), fails above B^* . The change occurring at B^* is evident in Fig. 4(b), which shows the first derivative of the longitudinal and Hall resistivities. The violet dotted lines demonstrate the apparent change of slope in MR and Hall resistivities at 14.5 T. We let $|n_h - n_e|$ to stay constant across B^* , in order to respect the Luttinger theorem [41]. We infer that F_2 and F_3 should correspond to carriers of opposite signs with a density difference of $|n_{F_3} - n_{F_2}| = 6.5 \times 10^{18} \text{ cm}^{-3}$. Assuming that there are 8 pockets for F_1 ($2n_{F_1} = 6.4 \times 10^{18} \text{ cm}^{-3}$), would be compatible with the Luttinger theorem. Both types of carriers increase by about $0.6 \times 10^{19} \text{ cm}^{-3}$ ($n_{F_3} - 2n_{F_1}$ and n_{F_2} , respectively). By fitting the Hall resistivity curve with $n_h = 4.9 \times 10^{19} \text{ cm}^{-3}$ and $n_e = 5.9 \times 10^{19} \text{ cm}^{-3}$, we obtain $\mu_h = 0.05(1) \text{ m}^2/\text{Vs}$ and $\mu_e = 0.16(1) \text{ m}^2/\text{Vs}$. This is shown in Fig. 4(c) with blue line. The mobility ($\mu = \frac{e\tau}{m^*}$) of holes drop ($\sim 72\%$) more than that of electron ($\sim 27\%$), implying the sign of F_1 with a small mass should be hole-like, since its mass increases by 2.5 times by assuming a same scattering time τ . We conclude that F_2 has an electron-like sign and F_3 is a

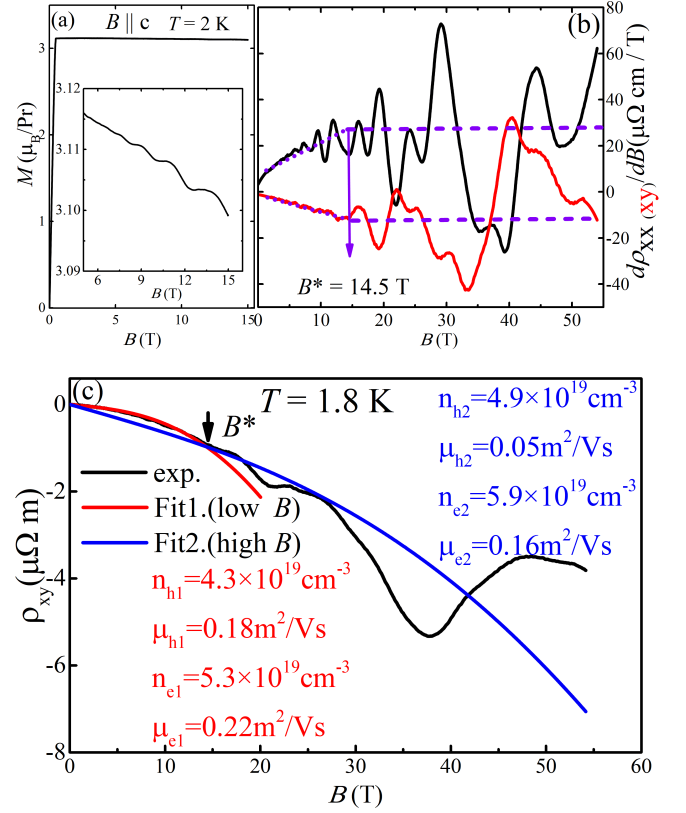


FIG. 4. (a) The magnetization of PrAlSi with the magnetic field applied along the c -axis, the inset is the enlarged part with evident QOs. (b) The black and red lines are the first derivative of the MR and Hall resistivities measured under pulsed field which could provide more information beyond the critical field. The violet dotted lines guided by eyes suggest the change of slopes in both of them at the B^* . (c) The field dependence of Hall resistance at 1.8 K along with two fitting curves with two-band model. The red and blue curves correspond to the fits to the low-field and high-field respectively.

hole-like one. Thus, each hole pocket (F_1) evolves into a larger hole pocket (F_3) and an additional electron pocket (F_2). This indicates the existence of a van-Hove singularity (saddle point) in this system.

To get more information about the Fermi surface of PrAlSi, we performed the measurements of angular-dependent MR with pulsed magnetic field at $T = 1.8 \text{ K}$. The Fig. 5 (a) shows the oscillatory component extracted by subtracting the smooth background from the MR measured at different θ , which is defined as the angle between the c axis and the magnetic field, and the current was along b axis as shown in the inset (see the Supplementary Figure 10 for the raw MR data). The SdH oscillations evolve systematically and can be observed in all angles as the magnetic field is rotated from $\theta = 0^\circ$ to $\theta = 87^\circ$. Fig. 5 (b) and Fig. 5 (c) present the segmented FFT spectra for different angles θ . The inset of figure

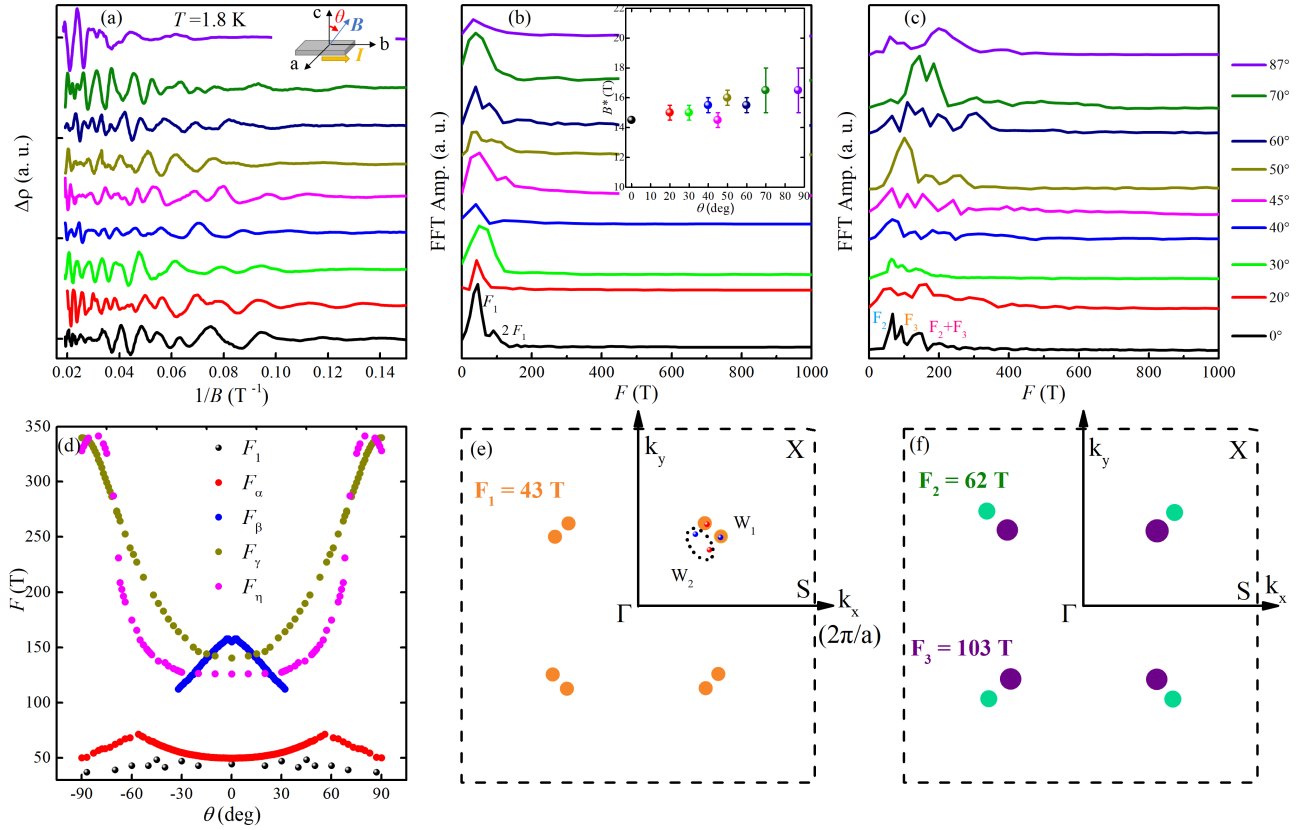


FIG. 5. (a) Background-subtracted SdH oscillatory part as a function of $1/B$ at $T = 1.8$ K under various angles. The inset on the top is the schematic diagram of the measurements. (b)(c) The FFT spectra for different angles and magnetic field ranges and the data are shifted along the vertical axis for clarity. The inset in graph (b) displays the critical fields of every angles and the error bars are defined as standard deviation. (b) The angular dependence of the corresponding measured oscillation frequency of F_1 pocket (black solid symbol) as well as the calculated frequencies F_α , F_β , F_γ and F_η . (e)(f) Schematic illustration of the Lifshitz transition in the BZ by the sketch of Fermi pockets which correspond to (b) and (c), respectively. Two tiny hole pockets (in orange) with $F_1 = 43$ T located along the sides of Γ -X transform into one electron pocket in green with $F_2 = 62$ T and one hole pocket in violet with $F_3 = 103$ T after LT, implying the existence of a van-Hove singularity. The pockets along Γ -S are not shown here (see the Supplementary Figure 9). In graph (e), the projection of two pairs of Weyl points around the Γ -X line in the BZ are illustrated, in which W_1 and W_2 are indicated. Weyl points with opposite chiralities are marked as red and blue dots.

(b) shows the critical fields at various angles, which indicating that the LT also involves with θ . We determined the B^* as the same method mentioned above and the detail is shown in Supplementary Figure 4. The oscillation frequency F_1 shown in Fig. 5 (b) is weakly dependent on angle, indeed indicating a nearly spherical Fermi surface of this band and the evolution of angle-dependent oscillation frequencies F_2 , F_3 and their harmonic terms shown in Fig. 5 (c). According to the experimental results, Fig. 5 (d) presents the angle dependence of the quantum oscillation F_1 which is shown as black symbols as well as F_α , F_β , F_γ and F_η are the calculated frequencies obtained from the SKEAF program [42]. The Fermi level was shifted with 3 meV in calculation because of the uncertain doping. The F_α is quite close to the observed F_1 . Whereas the higher frequencies obtained from calculation are not been observed by experiment in our case, may be due to the low mobility of these bands.

Next, we tried to locate these pockets in the BZ, and our similar calculation results (see the Supplementary Figure 11). The electronic structure also resembles that of NdAlSi [36]. Since the center of the BZ is not occupied, symmetry imposes four-fold degeneracy of each pocket. According to the calculation, the schematic of the positions of pockets F_1 , which are represented by orange spheres along the Γ -X direction of the BZ in Fig. 5 (e). The pockets along Γ -S are large and cannot be easily modified, hence for clarity they are not shown here and the Fermi pockets are plotted in the Supplementary Figure 9. Instead, the bands along Γ -X are shallow and host Weyl points and they should be susceptible to magnetic field. The new F_2 and F_3 pockets appear after the disappearance of F_1 . So it is a reasonable assumption that they locate on the Γ -X line as well where the pockets F_1 lie on, as shown in Fig. 5 (f). Indeed, some Weyl signatures were observed for the pockets F_1 . All the val-

ues extracted from the peak and valley positions of SdH oscillation fall on a line with an intercept of ~ 0.01 in the Landau fan diagram, indicating a non-trivial π phase (see the Supplementary Figure 6(b)). Its cyclotron mass is very small and changes with magnetic field. Note that a normal parabolic band ($E = \frac{\hbar^2 k^2}{2m}$) would not change its cyclotron mass ($m_{CR} = \frac{\hbar^2}{2\pi} \frac{\partial A_F(E, k_{\parallel})}{\partial E}$) [43] as the Fermi energy changes. The increasing of the effective mass may imply the increase of spin fluctuation of the pockets with LT transition, similar to the early report [14], instead of the response from a normal parabolic band. In order to better understand the Weyl nature of the Fermi pockets, it is indispensable for confirming the Weyl points along the direction of Γ -X line of the BZ. As shown in Fig. 5 (e), we obtained two pairs of Weyl points along the Γ -X line by band structure calculation of selected paths of the BZ and the details are listed in the table of Supplementary Figure 11. The results agree with the prior work on Weyl points and Fermi surface of PrAlSi [6].

Take together, three prominent features of the LT in PrAlSi can be found: (i) the QO frequencies are strongly temperature dependent, (ii) the quasiparticle effective mass increases gradually when approaching B^* , and (iii) the critical field for such LT is far below quantum limit. In conventional metals, only a small change in QO frequency of the order of $(k_B T / E_F)^2$ is expected upon warming [1]. Temperature-dependent QO frequency was observed in some HF metals, which is typically ascribed to the sensitivity of the f - c (c -conduction electrons) hybridization and the corresponding Kondo resonance state with a variation of temperature [2, 13?]. In this framework, the change of m^* was also attributed to an itinerant - localized transition of $4f$ electrons [14]. However, in PrAlSi, DFT calculations manifested that the Pr- $4f$ bands locate well below the Fermi level (see the Supplementary Figure 8), notable f - c hybridization is unlikely. Furthermore, PrAlSi is a low-carrier density semimetal, the Kondo screening is also expected to be weak according to Nozières exhaustion idea [47, 48]. Therefore, it is unlikely that the observed LT in PrAlSi originates from a competition between Zeeman term and a characteristic Kondo coherence energy as in HF systems. In the cases of bismuth [21], TaP [22] and TaAs [23], the quantum limits have been reached to empty a Dirac or Weyl pocket, and caused a field-induced LT. In our case, however, a rough estimate yields the quantum limit field in the range of 40-100 T, much larger than the critical field $B^* \sim 14.5$ T.

Another possibility for the observed LT in PrAlSi might be related to the crystal-electric-field (CEF) effect. This arises because the nine-fold-degenerate $j = 4$ multiplet of Pr^{3+} in a D_{2d} (42m) point symmetry CEF splits into two non-Kramers doublets and five singlets [49]. A recent analysis based on specific heat measurements revealed that the ground state is probably a doublet, while the magnetic entropy gain reaches $R \ln 3$ at about 20 K,

$R \ln 4$ at about 30 K, and saturates to $R \ln 9$ at a temperature as low as ~ 95 K [24]. This suggests that at least one excited state sitting not far above the ground doublet, potentially in the order of 10 K. It is reasonable to speculate that magnetic field of ~ 10 T might be sufficient to modify the CEF energy levels and the orbital characters, which possibly changes the Fermi surface topology. In addition, this field-induced evolution of CEF levels is also qualitatively consistent with the temperature-dependent QO frequency and field dependent m^* as observed experimentally. Actually, this scenario was also proposed recently for the field-induced Fermi surface reconstruction in CeRhIn₅ [50]. To further address this possibility, more experiments like inelastic neutron scattering are needed to figure out the diagram of the CEF splitting.

In summary, we grew high quality single crystals and observed pronounced SdH oscillations in PrAlSi with magnetic field up to 55 T. A LT transition occurs around 14.5 T. The change in carrier densities and Fermi pockets revealed by QO and Hall effect are consistent with each other. By comparison with theoretical calculations, we propose that LT occurs along the Γ -X orientation and involves the Weyl pockets. One hole pocket becomes an electron pocket and a hole pocket, which indicates the existence of a van-Hove singularity. PrAlSi, therefore, represents a unique case of field-induced LT beyond the HF systems.

*zhaolx@mail.sustech.edu.cn

*mpzslyk@hust.edu.cn

*zengwei.zhu@hust.edu.cn

DATA AVAILABILITY

The data supporting the present work are available from the corresponding authors upon request.

ACKNOWLEDGEMENTS

We thank Kamran Behina for insightful discussions. This work is supported by the National Key Research and Development Program of China (Grant No. 2022YFA1403503), the National Science Foundation of China (Grant Nos. 12004123, 51861135104 and 11574097), the Fundamental Research Funds for the Central Universities (Grant no. 2019kfyXMBZ071), the open research fund of Songshan Lake Materials Laboratory (2022SLABFN27) and National Key R&D Program of China (2022YFA1602602).

COMPETING INTERESTS

The authors declare no competing interests.

AUTHOR CONTRIBUTIONS

Z.Z. and L.Z. conceived and oversaw this work; L.W., H.Z. and L.Z. performed the experiments. Z.Z., G.X., L.W. and S.C. performed band-structure calculations. L.W., L.Z., Y.L. and Z.Z. wrote the manuscript with inputs from co-authors.

-
- [1] Lifshitz, I. Anomalies of electron characteristics of a metal in the high pressure region. *Sov. Phys. JETP* **11**, 1130–1135 (1960).
- [2] Varlamov, A. A., Galperin, Y. M., Sharapov, S. G. & Yerin, Y. Concise guide for electronic topological transitions. *Low Temp. Phys.* **47**, 672–683 (2021).
- [3] Steppke, A. *et al.* Strong peak in T_c of Sr_2RuO_4 under uniaxial pressure. *Science* **355**, 145 (2017).
- [4] Luo, Y. *et al.* Normal State ^{17}O NMR Studies of Sr_2RuO_4 under Uniaxial Stress. *Phys. Rev. X* **9**, 021044 (2019).
- [5] Yang, H. F. *et al.* Topological Lifshitz transitions and Fermi arc manipulation in Weyl semimetal NbAs. *Nat. Commun.* **10**, 3478 (2019).
- [6] Liu, Y. *et al.* Bond-breaking induced Lifshitz transition in robust Dirac semimetal VAl_3 . *Proc. Natl. Acad. Sci.* **117**, 15517 (2020).
- [7] Benhabib, S. *et al.* Collapse of the normal-state pseudogap at a Lifshitz transition in the $\text{Bi}_2\text{Sr}_2\text{CaCu}_2\text{O}_{8+\delta}$ cuprate superconductor. *Phys. Rev. Lett.* **114**, 147001 (2015).
- [8] Norman, M. R., Lin, J. & Millis, A. J. Lifshitz transition in underdoped cuprates. *Phys. Rev. B* **81**, 180513 (2010).
- [9] Ren, M. *et al.* Superconductivity across Lifshitz transition and anomalous insulating state in surface K–dosed $(\text{Li}_{0.8}\text{Fe}_{0.2}\text{OH})\text{FeSe}$. *Sci. Adv.* **3**, e1603238 (2017).
- [10] Liu, C. *et al.* Evidence for a Lifshitz transition in electron-doped iron arsenic superconductors at the onset of superconductivity. *Nat. Phys.* **6**, 419–423 (2010).
- [11] Kwon, J. *et al.* Lifshitz-transition-driven metal-insulator transition in moderately spin-orbit-coupled $\text{Sr}_{2-x}\text{La}_x\text{RhO}_4$. *Phys. Rev. Lett.* **123**, 106401 (2019).
- [12] Kozlova, N. *et al.* Magnetic-field-induced band-structure change in CeBiPt . *Phys. Rev. Lett.* **95**, 086403 (2005).
- [13] Aoki, D. *et al.* Field-induced Lifshitz transition without metamagnetism in CeIrIn_5 . *Phys. Rev. Lett.* **116**, 037202 (2016).
- [14] Aoki, H., Uji, S., Albessard, A. K. & Ōnuki, Y. Transition of f electron nature from itinerant to localized: Metamagnetic transition in CeRu_2Si_2 studied via the de Haas–van Alphen effect. *Phys. Rev. Lett.* **71**, 2110–2113 (1993).
- [15] Bastien, G. *et al.* Lifshitz transitions in the ferromagnetic superconductor UCoGe . *Phys. Rev. Lett.* **117**, 206401 (2016).
- [16] Yelland, E. A., Barraclough, J. M., Wang, W., Kamenev, K. V. & Huxley, A. D. High-field superconductivity at an electronic topological transition in URhGe . *Nat. Phys.* **7**, 890–894 (2011).
- [17] Niu, Q. *et al.* Fermi-surface instability in the heavy-fermion superconductor UTe_2 . *Phys. Rev. Lett.* **124**, 086601 (2020).
- [18] Pfau, H. *et al.* Interplay between Kondo suppression and Lifshitz transitions in YbRh_2Si_2 at high magnetic fields. *Phys. Rev. Lett.* **110**, 256403 (2013).
- [19] Pfau, H. *et al.* Cascade of magnetic-field-induced Lifshitz transitions in the ferromagnetic Kondo lattice material YbNi_4P_2 . *Phys. Rev. Lett.* **119**, 126402 (2017).
- [20] Gourgout, A. *et al.* Collapse of ferromagnetism and Fermi surface instability near reentrant superconductivity of URhGe . *Phys. Rev. Lett.* **117**, 046401 (2016).
- [21] Zhu, Z. *et al.* Emptying Dirac valleys in bismuth using high magnetic fields. *Nat. Commun.* **8**, 15297 (2017).
- [22] Zhang, C.-L. *et al.* Magnetic-tunnelling-induced Weyl node annihilation in TaP. *Nat. Phys.* **13**, 979–986 (2017).
- [23] Ramshaw, B. J. *et al.* Quantum limit transport and destruction of the Weyl nodes in TaAs. *Nat. Commun.* **9**, 2217 (2018).
- [24] Lyu, M. *et al.* Nonsaturating magnetoresistance, anomalous Hall effect, and magnetic quantum oscillations in the ferromagnetic semimetal PrAlSi . *Phys. Rev. B* **102**, 085143 (2020).
- [25] Chang, G. *et al.* Magnetic and noncentrosymmetric Weyl fermion semimetals in the RAlGe family of compounds (R=rare earth). *Phys. Rev. B* **97**, 041104 (2018).
- [26] Puphal, P. *et al.* Bulk single-crystal growth of the theoretically predicted magnetic Weyl semimetals RAlGe (R=Pr, Ce). *Phys. Rev. Mat.* **3**, 024204 (2019).
- [27] Nakatsuji, S., Kiyohara, N. & Higo, T. Large anomalous Hall effect in a non-collinear antiferromagnet at room temperature. *Nature* **527**, 212–215 (2015).
- [28] Kuroda, K. *et al.* Evidence for magnetic Weyl fermions in a correlated metal. *Nat. Mater.* **16**, 1090–1095 (2017).
- [29] Liu, E. *et al.* Giant anomalous Hall effect in a ferromagnetic kagome-lattice semimetal. *Nat. Phys.* **14**, 1125–1131 (2018).
- [30] Morali, N. *et al.* Fermi-arc diversity on surface terminations of the magnetic Weyl semimetal $\text{Co}_3\text{Sn}_2\text{S}_2$. *Science* **365**, 1286–1291 (2019).
- [31] Sakai, A. *et al.* Giant anomalous Nernst effect and quantum-critical scaling in a ferromagnetic semimetal. *Nat. Phys.* **14**, 1119–1124 (2018).
- [32] Su, H. *et al.* Multiple Weyl fermions in the noncentrosymmetric semimetal LaAlSi . *Phys. Rev. B* **103**, 165128 (2021).
- [33] Xu, S.-Y. *et al.* Discovery of lorentz-violating type II Weyl fermions in LaAlGe . *Sci. Adv.* **3**, e1603266 (2017).
- [34] Puphal, P. *et al.* Topological Magnetic Phase in the Candidate Weyl Semimetal CeAlGe . *Phys. Rev. Lett.* **124**, 017202 (2020).
- [35] Yang, H.-Y. *et al.* Noncollinear ferromagnetic weyl semimetal with anisotropic anomalous Hall effect. *Phys. Rev. B* **103**, 115143 (2021).
- [36] Gaudet, J. *et al.* Weyl-mediated helical magnetism in NdAlSi . *Nat. Mater.* **20**, 1650–1656 (2021).
- [37] Ding, L. *et al.* Intrinsic anomalous Nernst effect amplified by disorder in a half-metallic semimetal. *Phys. Rev. X* **9**, 041061 (2019).
- [38] Fauqué, B. *et al.* Magnetoresistance of semimetals: The case of antimony. *Phys. Rev. Mat.* **2**, 114201 (2018).
- [39] Bhargava, R. N. de Haas-van Alphen and galvanomagnetic effect in Bi and Bi-Pb alloys. *Phys. Rev.* **156**, 785–797 (1967).
- [40] Zhu, Z. *et al.* Quantum oscillations, thermoelectric coefficients, and the fermi surface of semimetallic WTe_2 . *Phys. Rev. Lett.* **114**, 176601 (2015).
- [41] Luttinger, J. M. Fermi surface and some simple equilibrium properties of a system of interacting fermions. *Phys. Rev.* **119**, 1153–1163 (1960).
- [42] Julian, S. Numerical extraction of de haas–van alphen frequencies from calculated band energies. *Comput. Phys. Commun.* **183**, 324–332 (2012).
- [43] Singleton, J. *Band theory and electronic properties of solids*, vol. 2 (Oxford University Press, 2001).
- [44] Yang, H.-Y. *et al.* Transition from intrinsic to extrinsic

- anomalous Hall effect in the ferromagnetic Weyl semimetal $\text{PrAlGe}_{1-x}\text{Si}_x$. *APL Mater.* **8**, 011111 (2020).
- [45] Shoenberg, D. *Magnetic oscillations in metals* (Cambridge university press, 2009).
 - [46] Goll, G. *et al.* Temperature-dependent fermi surface in CeBiPt. *EPL (Europhysics Letters)* **57**, 233 (2002).
 - [47] Nozières, P. Some comments on Kondo lattices and the Mott transition. *Eur. Phys. J. B* **6**, 447–457 (1998).
 - [48] He, X. *et al.* PrBi: Topology meets quadrupolar degrees of freedom. *Phys. Rev. B* **101**, 075106 (2020).
 - [49] Dhar, S. The heat capacity of PrSi_2 . *J. Magn. Magn. Mater.* **132**, 149–152 (1994).
 - [50] Lesseux, G. G. *et al.* Orbitally defined field-induced electronic state in a Kondo lattice. *Phys. Rev. B* **101**, 165111 (2020).

Supplementary information for “Field-Induced Lifshitz Transition in the Magnetic Weyl Semimetal Candidate PrAlSi”

S1. SAMPLES AND METHODS

Single crystals of PrAlSi used in our studies were synthesized using the flux method. The starting materials are high purity chunks of praseodymium, silicon and aluminum, mixed into an alumina crucible. Then, the alumina crucible and quartz wool were placed in a quartz tube, which was sealed under high vacuum, heated to 1100°C at 3°C/min. And holding for 12 h and then the tube was cooled down to 750°C in 100 h and dwells for 2 days. The excess Al flux was removed by centrifuging. To identify the as-grown sample quality of PrAlSi, powder crystal x-ray diffraction (XRD) was used. And, the single crystal XRD has been used to confirm the structure and the orientation of the single crystal. The results revealed the lattice parameters of the specimen are $a = b = 4.22\text{\AA}$, $c = 14.47\text{\AA}$, $\alpha = \beta = \gamma = 90^\circ$ with the tetragonal structure at room temperature. The atomic proportion was determined by energy dispersive x-ray spectroscopy (EDS). The sample for measurements with the dimension of $\sim 2 \times 0.5 \times 0.1\text{ mm}^3$ and the magnetic field was aligned along c -axis in all measurements. The low-field magnetic transport measurements were performed on an Integra AC (Oxford Instruments) with a 16 T superconducting magnet and a Leiden dilution refrigerator with a 14 T superconducting magnet. Temperature- and field-dependent resistivity measurements were made in the standard four-probe method with a pair of current source (Keithley 6221) and DC-Nanovoltmeter (Keithley 2182A). The high-field magnetic transport measurements were carried out under pulsed magnetic field in Wuhan National High Magnetic Field Center (WHMFC). Golden wires were attached using silver paste on the rectangular sample and the every contact resistance were maintained to be less than $2\ \Omega$ in the measurements.

The XRD pattern of the PrAlSi single crystal shown in Fig. S1(a) indicating the high quality sample in our measurement and the compositions of the synthesized crystals were analyzed using energy dispersive spectroscopy (EDS), showing in the Fig. S1(b). The XRD data in our work obtained from single crystal with selected plane (0 0 1) and in the previous studies (ref.[24] and ref.[43]) obtained from synthesized powder make the difference in the XRD patterns. The temperature - dependent of longitudinal resistivity $\rho_0(T)$ of the PrAlSi single crystal in the absence of an external magnetic field in this work was measured with the current applied along the b -axis ([010]), which showing a typical semimetal character, is presented in the Fig. S1(c). At high temperature, $\rho_0(T)$ displays the metallic behavior with an almost linear temperature dependence from 300 K and develops a small cusp at ferromagnetic transition $T_c = 17.8\text{ K}$ before further cooling to 2 K. The residual resistivity ratio RRR

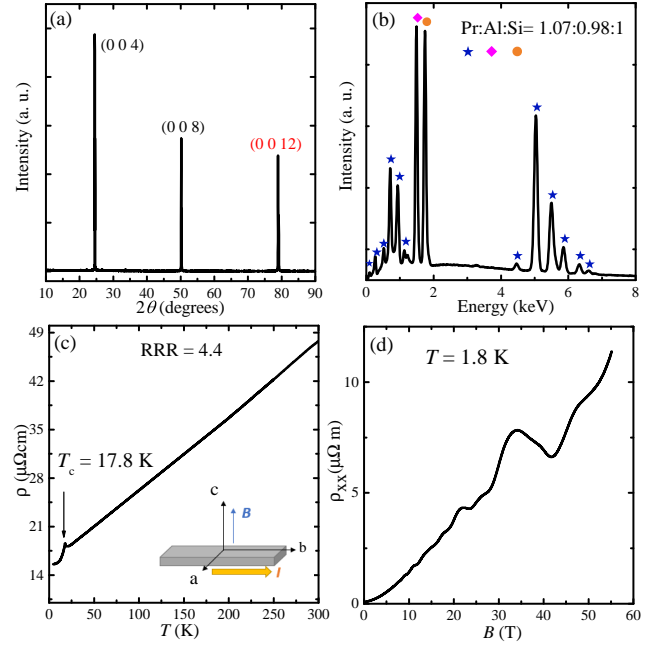


FIG. S1. (a) X-ray diffraction pattern of PrAlSi single crystal. (b) The diagram of the energy dispersive x-ray spectroscopy (EDS). (c) Temperature dependence of electrical resistivity from 2-300 K of the PrAlSi single crystal. The residual resistivity ratio $\rho(300\text{K})/\rho(2\text{K})$ is about 4.4. Inset is the configuration of the measurements. (d) Longitudinal resistivity as a function of magnetic field up to 55 T at 1.8 K.

which is defined as $\rho(300\text{K})/\rho(2\text{K})$ reaches the value of approximate 4.4 in our case. Fig. S1(d) displays the longitudinal magnetoresistivity up to $1140\ \mu\Omega\text{cm}$ under high magnetic field.

S2. RAW DATA OF THE FIELD DEPENDENCE OF MAGNETORESISTANCE AND AVERAGE MOBILITY

The temperature dependence of magnetoresistance of single crystal PrAlSi were measured under static field up to 14 T (Leiden dilution refrigerator) in Fig. S2(a) and up to 16 T (Oxford Instruments) in Fig. S2(b), respectively. Positive and unsaturated magnetoresistance and evident SdH oscillations under low temperature above 3 T are visible until up to 35 K in our measurements. The inset in (a) is the fitting result of $\text{MR} = \mu_{\text{ave}} B^2$ guided by the violet line and the obtained average mobility is $0.26\text{ m}^2/\text{Vs}$.

S3. DETAILS OF FFT ANALYSES

As mentioned above, the SdH QOs frequencies are discriminative with only one dominating frequency F_1 (43 T) below 14.5 T and another two higher frequencies

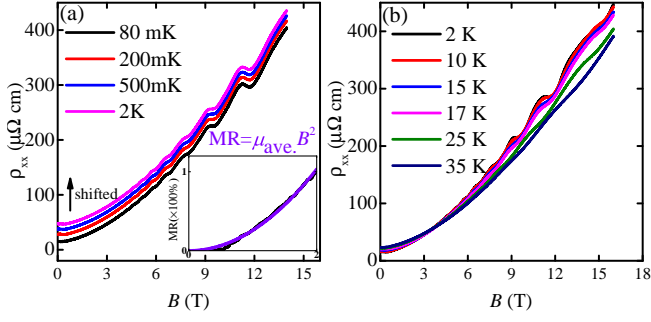


FIG. S2. (a) The temperature-dependent magnetoresistivity ρ_{xx} (shifted) measured from $T = 80$ mK to 2 K with magnetic field up to 14 T, the inset is the fitting result of the equation $MR = \mu_{ave} B^2$ with $\mu_{ave} = 0.26$ m²/Vs. (b) ρ_{xx} with the temperature variation from 2 K to 35 K as magnetic field up to 16 T.

F_2 (62 T) and F_3 (103 T) exist under higher field. We selected different low magnetic field ranges to analyze the FFT from the result of MR with $\theta = 0^\circ$ showing in Fig. S3. The FFT results accord with the discussion in Fig. 2, which indicating only one domain frequency under the critical magnetic field 14.5 T and the FFT peak becomes widely at 15 T and involves into another peaks when magnetic field increases up to 20 T eventually. This FFT analysis clearly shows the frequency variation as the function of magnetic field, we consider that 14.5 T (labelled with B^*) is indeed a critical point and the conclusion is well agreed with the two-band fitting of Hall resistivity in main text. In addition, in Fig. S4, similar to the method as mentioned above, the segmented FFT analyses with different angles (from 20° to 87°) were carried out and the results were summarized in the inset of Fig. 5(b).

S4. THE LIFSHITZ-KOSEVICH (LK) THEORY

As is known, the oscillatory part of magnetoresistance can be described by the LK formula[1] which is: $\Delta\rho = \sum_i A_i R_{Ti} R_{Di} \cos[2\pi(\frac{F_i}{B} - \delta_i)]$, where i is the number of Fermi pocket, A_i are prefactors, F_i are the oscillatory frequencies and δ_i are the phase factors. The $R_{Ti} = \alpha T m_i^* / B \sinh[\alpha T m_i^* / B]$ and $R_{Di} = \exp[\alpha T_{Di} m_i^* / B]$ are the thermal and scattered damping factors, where $\alpha = 2\pi^2 k_B m_e / e \hbar \simeq 14.69$ T/K, m^* is the cyclotron mass and T_{Di} is the Dingle temperature.

S5. FIELD DEPENDENCE OF MASS FOR THE F_1

As described in main text, the LT occurs around $B^* = 14.5$ T with the disappearance of a lower SdH frequency $F_1 = 43$ T. It's naturally to study the evolution of this Fermi pocket so that we extracted the effective mass as a function of magnetic field below B^* from the

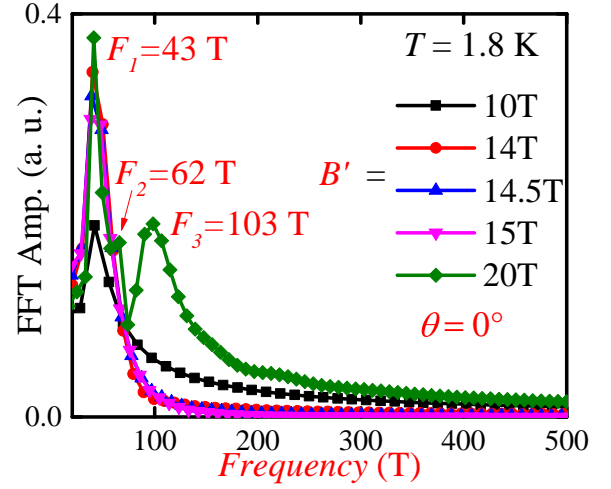


FIG. S3. The FFT analysis spectrum of MR in the reciprocal fields from 5.7 T to the selected magnetic field B' near B^* , measured in pulsed field.

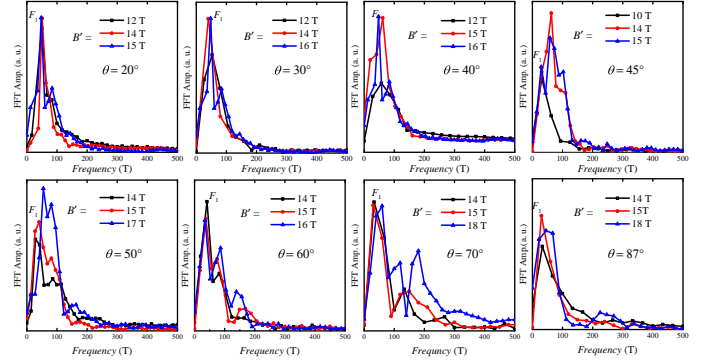


FIG. S4. The FFT analysis spectrum of MR in the reciprocal fields from 8 T to the selected magnetic field B' at different angles.

temperature dependence of the SdH oscillatory components at different fields as shown in the Figure. S5. We can extract m^* from the SdH peaks directly because it relates to the temperature damping factor which is evident reflecting in the SdH oscillation component showing in Figure. S5 (a). In addition, the effective masses of the Fermi pockets mentioned in Fig. 2, which were extracted from the amplitude of temperature-dependent FFT spectra, are plotted in Figure. S5 (b).

S6. QUANTUM OSCILLATION PHASE FACTOR ANALYSIS FOR F_1

In order to pin down the property of the topological state in PrAlSi, the Landau level (LL) index fan diagram, which could manifest the nontrivial φ_B in Weyl system, is much essential. The oscillatory component $\Delta\rho$ at 2

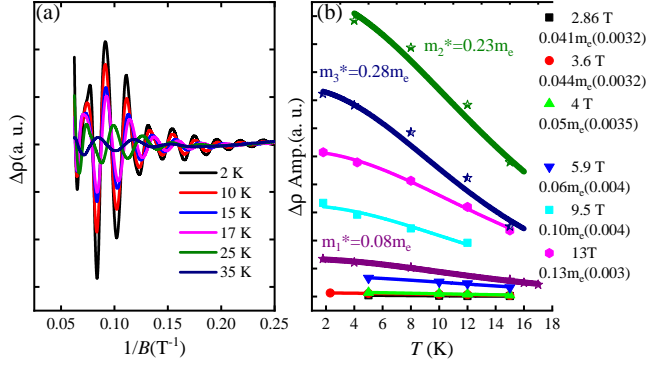


FIG. S5. (a) The SdH oscillatory component as a function of $1/B$ after subtracting the smoothed background from 2 K to 35 K measured under static field with magnetic field up to 16 T. (b) Effective masses of F_1 as a function of magnetic field below B^* extracted from the temperature-dependent SdH amplitude of peaks by fitting with the damping factor in the LK function are summarized in the Fig. 2(c). Besides, the cyclotron mass m^* of F_1 was extracted by fitting the FFT amplitude of SdH oscillations (Fig. 2(a)) to the temperature damping factor of the LK equation from 5.7 T to 14.5 T, and the same method for F_2 and F_3 with field from 14.5 T to 55 T.

K under static field is obtained by subtracting the background and plotted as the function of $1/B$ in Figure. S6 (a). An apparent simple pattern here is in accordance with the discussion of Fig. 1 in main text indicating the single main frequency under low magnetic field range in QOs pattern. According to the LK formula:

$$\Delta\rho \sim \frac{\lambda T}{\sinh(\lambda T)} e^{-\lambda T_D} \cos[2\pi(\frac{F}{H} - \frac{1}{2} + \delta)] \quad (\text{S1})$$

Here, the phase factor is $\delta - \frac{1}{2} = \frac{\varphi_B + \varphi_D}{2\pi} - \frac{1}{2}$, where φ_B is Berry phase and φ_D equals $\pm \frac{1}{8}$ which depends on the cross-section extremum with maximal or minimal for 3D cases. Figure. S6 (b) displays the Landau level (LL) fan diagram for the fundamental frequency F_1 . Here, the minimum $\Delta\rho$ (red) is integer indices and the maximum $\Delta\rho$ (black) is half-integer indices. All points are well linearly fitting and we extrapolate $1/B$ to zero and obtain the intercept is $-0.01 = \delta - \frac{1}{2}$, indicating a π Berry phase and non-trivial topological state of the F_1 in PrAlSi single crystal.

S7. TWO-BAND FITTING FOR THE MAGNETORESISTIVITY ρ_{xx} AND HALL CONDUCTIVITY σ_{xy}

ρ_{xx} and σ_{xy} in our case can be described by the two-band model:

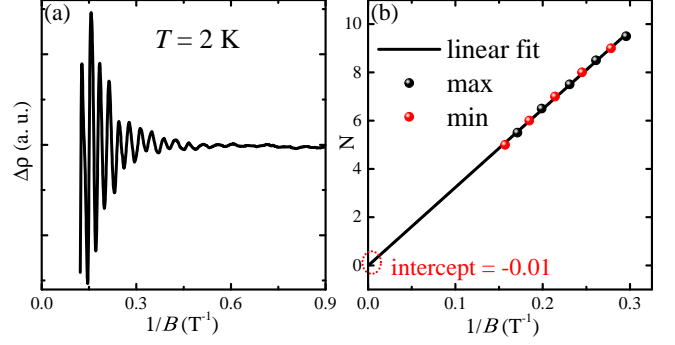


FIG. S6. (a) $\Delta\rho$ as the function of B^{-1} at indicated temperature. (b) Landau level fan diagram of F_1 extracted from $\Delta\rho$ and the line indicates the linear fitting to the data. The solid circles represent the maxima and minima of $\Delta\rho$, respectively.

$$\rho_{xx} = \frac{1}{e} \frac{(n_h \mu_h + n_e \mu_e) + \mu_h \mu_e (n_e \mu_h + n_h \mu_e) B^2}{(n_h \mu_h + n_e \mu_e)^2 + \mu_h^2 \mu_e^2 (n_h - n_e)^2 B^2} \quad (\text{S2})$$

$$\sigma_{xy} = eB \left(\frac{n_h \mu_h^2}{1 + \mu_h^2 B^2} - \frac{n_e \mu_e^2}{1 + \mu_e^2 B^2} \right) \quad (\text{S3})$$

Here, n_h (n_e) and μ_h (μ_e) are carrier concentration and mobility for the holes (electrons), respectively. The fitted result of magnetoresistivity ρ_{xx} with the parameters identical with the main text shows a good fit in low field range up to B^* shown in Figure. S7 (a) in red, while the experimental curve is in black. The fitted result of Hall conductivity σ_{xy} indicates carrier concentration are $n_h = 1.5 \times 10^{20} \text{ cm}^{-3}$ ($n_e = 1.6 \times 10^{20} \text{ cm}^{-3}$) and the corresponding mobilities are $\mu_h = 0.86 \text{ m}^2/\text{Vs}$ ($\mu_e = 0.81 \text{ m}^2/\text{Vs}$). The field dependence of Hall conductivity shows a sharp rise in the low fields and slowly decrease as the field is increased. The fitting is tricky and a little change in the parameters would not change the fitting result, especially in the high-field range. So we fit the Hall resistance which has much better shape for the fitting,

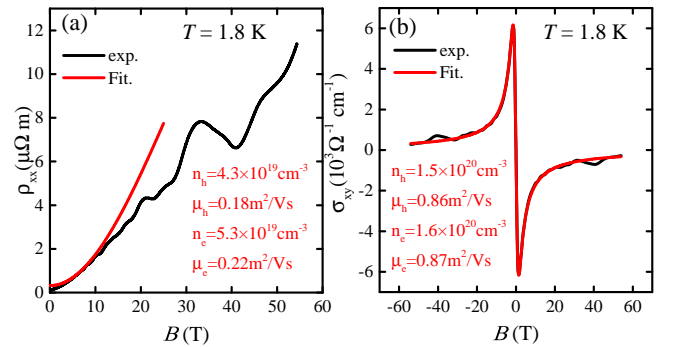


FIG. S7. (a) and Hall conductivity (b) of PrAlSi at 1.8 K. The black solid line is the experimental data and the red solid line is the fitted curve with two-band model, respectively.

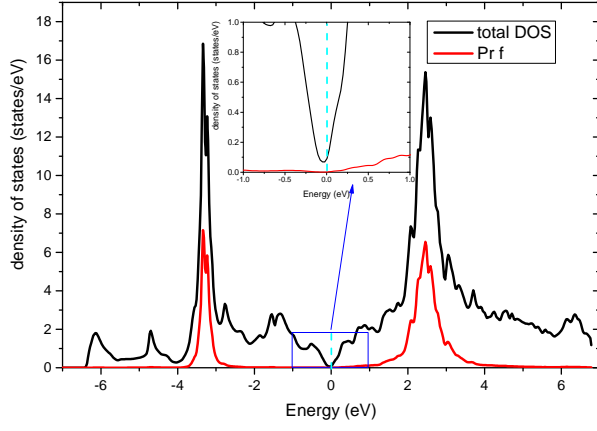


FIG. S8. The total density of states and the density of states (DOS) of f orbit.

giving more convincing results. Besides, the obtained carriers 1.5×10^{20} (1.6×10^{20}) cm^{-3} for holes (electrons) lead to a mobility of $0.17 \text{ m}^2/\text{Vs}$ at zero field, which is quite distinct from the fitting results of $\sim 0.9 \text{ m}^2/\text{Vs}$.

S8. THE COMPARISON OF HALL RESISTIVITY WITH CEBIPT

In CeBiPt, LT promotes carrier density from $7.2 \times 10^{17} \text{ cm}^{-3}$ to $9.2 \times 10^{17} \text{ cm}^{-3}$, increased by 28%. The change of PrAlSi is mainly in mobility beyond after LT, with 75% for holes and 27% for electrons. The large drop of mobility is most likely due to the increase of inter-bands scattering because of more pockets present after LT and also the increase of mass of the pockets. The drops in mobility may result in the downward of MR above LT in the Fig. 1(a). The sub-linear Hall resistance is single-band behavior in CeBiPt[2], while it is a multi-band behavior in PrAlSi and has two-order higher carriers concentration and mainly changes its mobility. Thus, one can clearly observe the linearity change of Hall resistance in CeBiPt, while smooth evolution of Hall resistivity and an evident deviation in first derivative of Hall resistivity in the current case. The same feature is that no sudden change occurs in Hall resistance during LT.

S9. INTERNAL FIELD AND EXTERNAL FIELD

PrAlSi is a ferromagnet with the $T_c = 17.8 \text{ K}$ (Fig. S1(c)). We considered its demagnetization factor and external field to infer the internal field which exerts on carriers. The internal field $B_{int} = \mu_0 H_{ext} + \mu_0(1 - n)M$, where n is the demagnetization factor. According to the report [3], $n = 0.77$ of our rectangular sample is obtained by fitting the shape factor into the given function. $\Delta B = B_{int} - B_{ext} = 0.23\mu_0 M_{exp} = 0.46 \text{ T}$, here $\mu_0 = 1.257 \times 10^{-6} \text{ H/m}$.

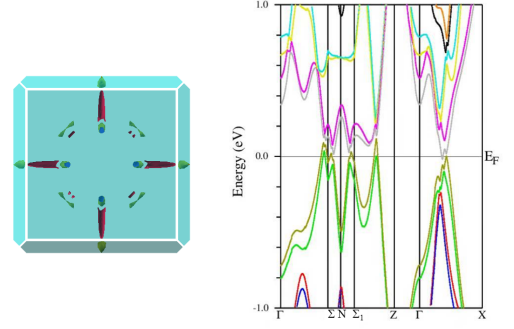


FIG. S9. The first-principle calculation results. (a) The calculated Fermi surface and (b) band structure of the PrAlSi.

S10. THE DOS OF PR F ELECTRON

The Fig. S8 shows the total density of states and the density of states (DOS) of f orbit from Pr in the energy scale of -7 to 7 eV. And the inset shows the enlarged part for the energy scale of -1 to 1 eV. All the f electrons of Pr are clearly below Fermi level and do not contribute to the conductivity on the Fermi surface. So we will not expect $f - c$ (c -conduction electrons) hybridization in the system.

S11. THEORETICAL CALCULATION

The theoretical calculation was carried out with WIEN2k which is based on the density functional theory

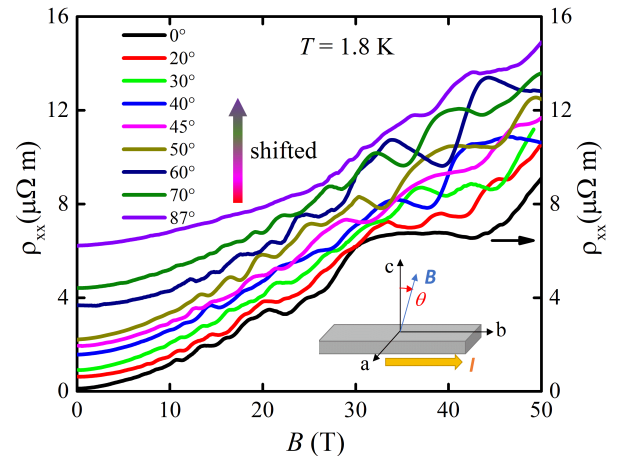


FIG. S10. Isothermal magnetoresistance measured at different angles. The magnetic field dependence of the resistivity with $\theta = 0^\circ$ follows the right scale and the curves of other angles were shifted as the arrow indicated. Inset is the configuration of the measurements.

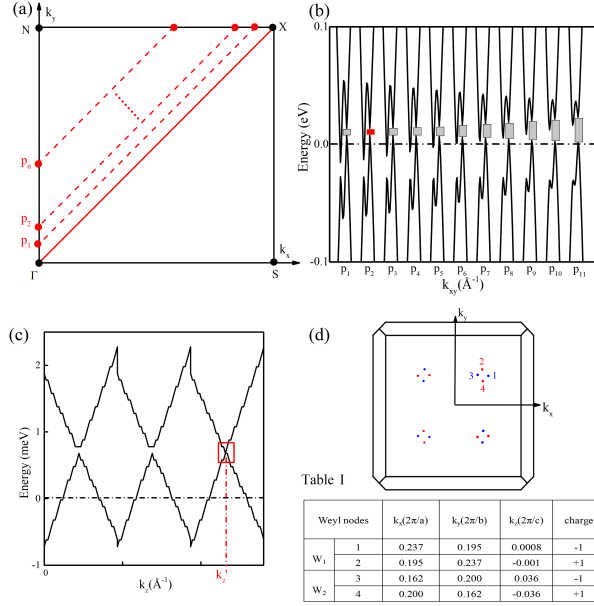


FIG. S11. (a), (b) and (c) introduce the process of band calculation for obtaining the Weyl point 1 showing in Fig. S11(d). (a) A diagram introduces the selective paths which are parallel to the Γ -X direction (in the plane with $k_z = 0$) in the calculation in detail. (b) The results of the calculated band structure according to the paths showing in graph (a) with different values of k_x, k_y and the rectangle in red indicates the projected position of the Weyl point. (c) Further calculation with only changing k_z for getting the gapless point (the exact value of k'_z) labeled by the red rectangle. (d) The four key Weyl points are illustrated in the sketch. Table I presents the specific position of nodes 1-4.

(DFT) based linearized augmented plane wave (LAPW) method[4]. We used the Perdew-BurkeErnzerhof (PBE) generalized gradient approximation (GGA)[5] form of the exchange correlation function. The RKmax was set to 5 which is determined by the smallest atom Si[4]. The results are for the effective Hubbard U of 6 eV by taking the on-site correlation using the DFT+U approximation for the f state of Pr. The spin-orbit coupling was included in “second variation” of the calculation. The calculated results are consistent with the reported[6], shown in the

Fig. S9, plotted by XcrysDen[7]. Along Γ -X direction in the Fig. S9 (a), the small pockets located on the sides of the direction have 8 pockets, which could be the F_1 . The calculated band structure shown in the Fig. S9 (b) is also well consistent with the reported. Along Γ -X direction, the bands are shallow and could be source of the instability during the LT process. In Fig.5(d) of the main text, the data at the angles larger than 60° are the average values because of the data calculated from the SKEAF program were noisy, which probably due to the insufficient k -points in the calculation.

S12. RAW DATA OF MR AT DIFFERENT TILT ANGLES θ

The angle dependence of quantum oscillations at different angles would provide much information of Fermi surface, such as shape and dimensionality. Fig. S10 shows magnetoresistance at different θ values with pulsed field at 1.8 K. A shifted figure was shown to clarify the MR with tilted angles. As seen, all the magnetoresistance are positive with the increasing angles and the oscillations are evident, which indicating a 3D feature of the Fermi surface.

S13. WEYL POINTS ASCERTAINING BY BAND STRUCTURE CALCULATION

The first step in our case is to address the points in k_x - k_y plane with $k_z = 0$, where the tiniest gap band occurs. Fig. S11 (a) is a rough schematic diagram with the paths of the band calculation. The red solid and dotted lines are the equally spaced paths in the direction parallel to the Γ -X line of the BZ. The results of calculated band structure are shown in Fig. S11 (b) with red rectangular frame indicating the approximate path, where the Weyl points locate. And then, as Fig. S11 (c) shown, changing the values of k_z for getting the gapless points to ensure accurate position of the Weyl points. Clearly, the Weyl point 1 is of hole nature. Fig. S11 (d) shows the partial Weyl points in the first Brillouin zone and the corresponding positions in k -space of the points (1-4) are listed in Table I.

Table I

Weyl nodes	$k_x(2\pi/a)$	$k_y(2\pi/b)$	$k_z(2\pi/c)$	charge
W_1	1	0.237	0.195	0.0008
	2	0.195	0.237	-0.001
W_2	3	0.162	0.200	0.036
	4	0.200	0.162	-0.036

[1] Shoenberg, D. *Magnetic oscillations in metals* (Cambridge university press, 2009).
[2] Kozlova, N. *et al.* Magnetic-field-induced band-structure change in CeBiPt. *Phys. Rev. Lett.* **95**, 086403 (2005).
[3] Aharoni, A. Demagnetizing factors for rectangular ferromagnetic prisms. *Journal of Applied Physics* **83**, 3432–3434.
[4] Blaha, P. *et al.* Wien2k: An apw+lo program for calculating the properties of solids. *The Journal of Chemical Physics* **152**, 074101 (2020).

[5] Perdew, J. P., Burke, K. & Wang, Y. Generalized gradient approximation for the exchange-correlation hole of a many-electron system. *Physical Review B* **54**, 16533–16539 (1996).
[6] Yang, H.-Y. *et al.* Transition from intrinsic to extrinsic anomalous Hall effect in the ferromagnetic Weyl semimetal PrAlGe_{1-x}Si_x. *APL Materials* **8**, 011111 (2020).
[7] Kokalj, A. Xcrysden—a new program for displaying crystalline structures and electron densities. *Journal of Molecular Graphics and Modelling* **17**, 176–179 (1999).